with an electronic structure complex enough to maximize $d[\ln \sigma(E)]/dE$ will be a good candidate for consideration.

12. M. G. Kanatzidis *et al.*, *Chem. Mater.* **8**, 1465 (1996); B. Chen, C. Uher, L. Iordanidis, M. G. Kanatzidis, *Chem. Mater.* **9**, 1655 (1997).
13. D.-Y. Chung *et al.*, *Chem. Mater.* **9**, 3060 (1997).
14. D.-Y. Chung *et al.*, *Proceedings of the 16th International Conference on Thermoelectrics* (Dresden, Germany, 1997), p. 459.
15. J. L. Schindler *et al.*, *Mater. Res. Soc. Symp. Proc.* **478**, 327 (1997).
16. Single-crystal x-ray diffraction data for $CsBi_4Te_6$ were collected at 293 K on a Siemens SMART Platform charge-coupled device diffractometer. Data are as follows: monoclinic $C2/m$ (no. 12); $a = 51.9205 \pm 0.0008$ Å, $b = 4.4025 \pm 0.0001$ Å, $c = 14.5118 \pm 0.0003$ Å, $\beta = 101.480 \pm 0.001°$, $Z = 8$, $V = 3250.75 \pm 0.11$ Å^3, $d_{calc} = 7.09$ g/cm^3; $\mu = 55.90$ mm^{-1}, $1.43° < \theta$ (Mo K_α) $< 28.17°$; total reflections, 18,450; unique reflections, 4373 [$R_{int} = 0.0767$]; final R indices for all data, $R_1 = 0.0585$, $_wR_2 = 0.1127$. The structure solution and refinements were done using the SHELXTL package of crystallographic programs (version 5, 1994; G. M. Sheldrick, Siemens Analytical Xray Systems Inc., Madison, WI).
17. Electronic band structure calculations at the density functional theory level are under way (P. Larson, S. D. Mahanti, D.-Y. Chung, M. G. Kanatzidis, in preparation).
18. Fractional atomic coordinates ($\times 10^4$) and equivalent atomic displacement parameters (10^3 Å^2) for $CsBi_4Te_6$ with estimated standard deviations in parentheses (atom, x, y, z, B_{eq}) are as follows: Bi(1), 1362(1), 0, 7502(1), 17(1); Bi(2), 2124(1), 5000, −888(1), 18(1); Bi(3), 1628(1), 0, 921(1), 18(1); Bi(4), 886(1), 5000, −627(1), 18(1); Bi(5), 2353(1), 5000, −7410(1), 17(1); Bi(6), 1146(1), 5000, 2782(1), 17(1); Bi(7), 150(1), 0, 7878(1), 18(1); Bi(8), 396(1), 0, 1365(1), 18(1); Cs(1), 543(1), 0, 5090(1), 26(1); Cs(2), 3130(1), 0, −5163(1), 28(1); Te(1), 1533(1), 5000, −722(1), 14(1); Te(2), 800(1), 0, 7845(1), 16(1); Te(3), 1226(1), 5000, 6089(1), 18(1); Te(4), 2020(1), 0, 7561(1), 16(1); Te(5), 2250(1), 0, 766(1), 14(1); Te(6), 1043(1), 0, 1003(1), 15(1); Te(7), 1757(1), 5000, −7570(1), 16(1); Te(8), 1236(1), 0, 4213(1), 18(1); Te(9), 2396(1), 0, −5982(1), 18(1); Te(10), 575(1), 5000, 2811(1), 18(1); Te(11), −76(1), 5000, 3592(1), 19(1); Te(12), 322(1), 5000, −383(1), 17(1).
19. G. A. Slack, in *CRC Handbook of Thermoelectrics*, D. M. Rowe, Ed. (CRC Press, Boca Raton, FL, 1995), p. 407; G. A. Slack, in *Solid State Physics*, H. Ehrenreich, F. Seitz, D. Turnbull, Eds. (Academic Press, New York, 1997), vol. 34, p. 1.
20. J. W. Lyding, H. O. Marcy, T. J. Marks, C. R. Kannewurf, *IEEE Trans. Instrum. Meas.* **37**, 76 (1988).
21. Variable-temperature (4.2 to 295 K) thermopower data were taken using a slow-ac measurement technique. The measurement apparatus featured Au (0.07% Fe)/Chromel differential thermocouples for monitoring the applied temperature gradients. Samples were mounted on 60-μm gold wire using gold paste. Fine gold wire (diameter 10 μm) was used for sample voltage contacts, which were made as long as possible to minimize thermal conduction through the leads. The sample and thermocouple voltages were measured using Keithley Model 181 and Model 182 nanovoltmeters, respectively. The applied temperature gradient was about 0.1 to 0.4 K. Measurements were taken under a turbo-pumped vacuum maintained below 10^{-5} torr. The sample chamber was evacuated for at least 1 hour before cooling to remove any residual water vapor or solvents in the gold paste.
22. The density of oriented ingots is >99% of theoretical density. The thermal conductivity was measured along the growth direction, which is the direction of maximum TE performance.
23. H. J. Goldsmid and J. W. Sharp, *J. Electron. Mater.* **28**, 869 (1999).
24. No significant variations (to ±10%) in thermal conductivity were observed between hot-pressed and oriented ingot samples.
25. *Encyclopedia of Materials Science and Engineering* (MIT Press, Cambridge, MA, 1986), p. 4968.
26. C. Kittel, in *Introduction to Solid State Physics* (Wiley, New York, ed. 6, 1986), p. 150.
27. M. V. Vedernikov, V. A. Kutasov, L. N. Luk'yanova, P. P. Konstantinov, in *Proceedings of the 16th International Conference on Thermoelectrics* (Dresden, Germany, 1997), p. 56.
28. H. Süßmann and W. Heiliger, in *Proceedings of the Conference on Transport in Compound Semiconductors* (MLU, Halle, Germany, KTB series 1982), p. 100.
29. P. Larson, S. D. Mahanti, D.-Y. Chung, M. G. Kanatzidis, in preparation.
30. Supported by Office of Naval Research grant N00014-98-1-0443. The work made use of the SEM facilities of the Center for Electron Optics at Michigan State University. The work at Northwestern made use of the Central Facilities supported by NSF through the Materials Research Center (grant DMR-9632472). We thank S. D. Mahanti for fruitful discussions.

20 September 1999; accepted 10 December 1999

Physics of Iron at Earth's Core Conditions

A. Laio,[1] S. Bernard,[2] G. L. Chiarotti,[1]* S. Scandolo,[1,3] E. Tosatti[1,3]

The bulk properties of iron at the pressure and temperature conditions of Earth's core were determined by a method that combines first-principles and classical molecular dynamic simulations. The theory indicates that (i) the iron melting temperature at inner-core boundary (ICB) pressure (330 gigapascals) is 5400 (±400) kelvin; (ii) liquid iron at ICB conditions is about 6% denser than Earth's outer core; and (iii) the shear modulus of solid iron close to its melting line is 140 gigapascals, consistent with the seismic value for the inner core. These results reconcile melting temperature estimates based on sound velocity shock wave data with those based on diamond anvil cell experiments.

Iron is thought to be the main constituent of Earth's solid inner core and liquid outer core. However, the bulk properties of Fe at such extreme physical conditions remain uncertain, including (i) the Fe melting temperature T_m at the pressure of the ICB (330 GPa) (*1–6*); (ii) the density of liquid Fe at T_m, which is needed to determine whether elements lighter than Fe are present in the outer core (*7–10*); and (iii) the elastic behavior of solid Fe close to the melting line (*11–14*).

The Fe melting temperature at high pressures has been determined by diamond anvil cell (DAC) and shock wave experiments (*1–6*). Recent DAC estimates of the melting line extend to 190 GPa (*3*) and agree with each other (*5, 6*) within 500 K. Shock wave–based estimates are available at ~240 GPa, but these result in a wider range of possible melting temperatures of 5800 K (*1*), 6700 K (*2*), and 6350 K (*4*). All of the shock wave–based estimates for T_m are inconsistent with the extrapolation of the Fe melting line from static DAC experiments (*3*), which predict a T_m of ~4000 K at 240 GPa.

We calculated the properties of Fe by a method that combines first-principles and classical molecular dynamics (MD) simulations. A correct account of the electronic structure of Fe at the ab initio level is fundamental for an accurate and reliable description of the properties of Fe at Earth's core conditions (*13, 15–17*). Our calculations were based on a finite-temperature extension of density-functional theory within the gradient-corrected local density approximation (GC LDA) (*18*) and on a pseudopotential description of the valence electron interaction with the ion core (nucleus plus 1s, 2s, and 2p atomic core states) (*19*). The calculated low-temperature pressure-density curve for hexagonal close-packed (hcp) Fe agrees with the x-ray data (*20*) (first-principles densities are ~1% smaller than experimentally determined densities at all pressures).

First-principles quality information on the high-temperature properties of Fe (melting properties, elasticity, diffusion, and Hugoniot equation of state) was obtained in this work by constructing classical potentials with an explicit dependence on the thermodynamic pressure-temperature (P-T) condition, exactly mimicking the first-principles MD at that P-T point. The potential, which includes non–two-body terms (*21, 22*) and angular forces (*22*), is optimized by matching the classical and first-principles forces and stresses with a self-consistent iterative procedure (*23*). Thermodynamic properties at that P-T condition are then extracted from classical MD simulations. The optimal potential (OP) constructed in this way will not be transferable to a different P-T condition, where a different potential must be constructed. Our approach is thus different from previous attempts to estimate the melting temperature

[1]International School for Advanced Studies and Istituto Nazionale per la Fisica della Materia, Via Beirut 2/4, I-34014 Trieste, Italy. [2]Commissariat à l'Energie Atomique, DRIF, BP 12, F-91680 Bruyères la Châtel, France. [3]International Centre for Theoretical Physics, I-34014 Trieste, Italy.

*To whom correspondence should be addressed. E-mail: guido@sissa.it

through classical MD studies (*21, 24*), where a single potential was used at all *P-T* conditions. Here, the essential coincidence of forces and stresses with first-principles ones at any given *P-T* point guarantees ab initio quality to the results. Our method also differs from a recent determination of T_m by first-principles thermodynamic integration (*25*) because it allows us to overcome the size and time-scale limitations typical of first-principles simulations.

The overall predictivity of our theoretical approach was tested by calculating the melting properties of Al at ambient pressure (*26*), where well-constrained experimental data are available. Our approach gives a melting temperature (*27*) for Al at ambient pressure of 940 ± 30 K [experimental data, T_m = 933 K (*28*)], a liquid density ρ at T_m of 2.37 ± 0.02 g/cm^3 [experimental data, 2.375 g/cm^3 (*28*)], a density increase at the melting point of $\Delta\rho/\rho$ = 6.1 ± 0.2% [experimental data, 6.6% (*28*)], and an entropy of melting $\Delta S = 1.18\ (\pm 0.10)k_B$ [experimental data $1.38k_B$ (*28*)] (k_B is the Boltzmann constant), leading, through the Clausius-Clapeyron law, to a melting slope of 71 (±8) K/GPa [experimental data, 65 K/GPa (*29*)]. For Al, our agreement with experimental data at melting is similar to that obtained with first-principles thermodynamic integration on the same system (*30*).

Particular attention has been devoted to the analysis of the error bars on our calculated values. These are of two types: (i) errors introduced by the OP modeling of the first-principles dynamics and (ii) errors intrinsic to the first-principles calculations on which the OP construction is based. In the case of Fe at Earth's core conditions, the second type of errors is larger than the first type of errors.

A measure of how accurately the OP modeling reproduces the first-principles thermodynamic observables at *P-T* is given by the difference between the OP and first-principles free energies $\delta F = F_{OP}(P,T) - F_{FP}(P,T)$. In particular, the error on T_m introduced by the OP modeling is related to the errors

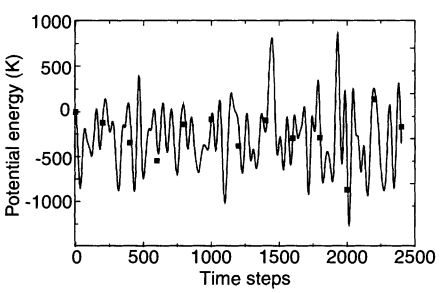

Fig. 1. Comparison between OP and first-principles potential energies per atom for Fe. The curve represents potential energy calculated along a MD trajectory generated with an OP optimized at 200 GPa and 4200 K. Squares indicate first-principles total energy computed at intervals of 200 time steps along the same trajectory.

$\delta F^{s,l}$ in the free energy of the liquid (l) and solid (s) phases as $|\delta T_m|\Delta S \simeq |\delta F^l - \delta F^s| < |\delta F^l| + |\delta F^s|$. Because the first-principles potential energy U_{FP} is similar (Fig. 1) to the OP one (U_{OP}), δF can be calculated as $\delta F \simeq \langle U_{OP} - U_{FP} \rangle$ (*31*), where the average is calculated on an OP MD trajectory. From Fig. 1 (and a similar calculation for the liquid phase), we calculate, assuming $\Delta S \sim 1k_B$, that $\delta T_m \sim 100$ K (*32*).

A second source of error comes from the finite size of the first-principles simulation cell. This has been estimated by repeating the full procedure with cells of increasing size, for selected *P-T* points. For P = 330 GPa, the melting properties were calculated (*27*) with OPs generated using first-principles cells containing 64 and 128 atoms. The resulting T_m, ρ, Δρ, and ΔS are unchanged (within the errors associated with the OP modeling) when going from 64 to 128 atom cells. Such convergence is similar to that observed in the case of Al (*26*).

A third source of errors may arise because of a different accuracy of the GC LDA in describing the solid and the liquid. As is customary in first-principles calculations, errors due to the GC LDA can only be assessed by comparison with experiments. As for errors in T_m, we considered that (i) where T_m is known, as in Al, the T_m calculated within the LDA is accurate; (ii) free-energy differences on Fe at T = 0 K are accurately described by the GC LDA (*16*); and (iii) others (*25*) have estimated the error on T_m associated with the GC LDA for Fe to be ±300 K. We followed the error analysis presented in (*25*) and assigned to the error associated with the GC LDA a value of, at most, ±300 K. In conclusion, our estimate of T_m should be affected by an overall error of ±400 K. As for errors in density, our calculated values

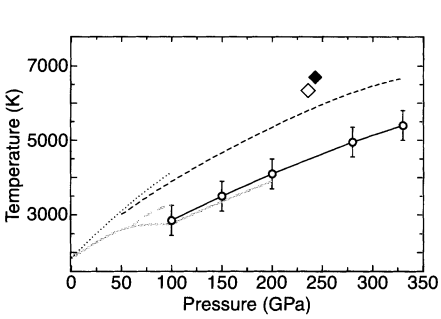

Fig. 2. High-pressure melting curve of Fe. Our results are given by open circles with error bars (bars in Figs. 2 and 5 represent errors discussed in text). The gray solid curve shows DAC data by Boehler (*3*) and data (up to ~150 GPa) by Saxena *et al.* (*5*); the gray dashed curve shows DAC data by Shen *et al.* (*6*). The dotted line indicates DAC data by Williams *et al.* (*2*); the dashed line indicates theoretical results by Alfè *et al.* (*25*). The open diamond shows shock wave datum by Yoo *et al.* (*4*), and the solid diamond shows shock wave datum by Williams *et al.* (*2*).

are ~1% smaller than the experimental ones in the solid and the liquid phases; this error is systematic and does not affect the density differences.

The calculated melting line of hcp Fe [ε phase (*6*)] from 100 to 330 GPa (Fig. 2) agrees, within the error bars, with recent laser-heated DAC experiments (*3, 5, 6*), with a slightly better agreement with data from (*3*) and (*5*), available up to 190 and 150 GPa, respectively. At the ICB pressure (330 GPa), we find that the hcp Fe melts at 5400 K, higher than Boehler's extrapolation of the melting point at 330 GPa (4900 K) (*3*). As shown below, our melting line is also consistent with Brown and McQueen's shock wave data (*1*). The melting temperatures recently calculated by first-principles thermodynamic integration (*25*), the earlier DAC measurements by Williams *et al.* (*2*), and that extracted from direct temperature measurements in shock wave experiments (*2, 4*) are higher than our results at any pressure.

To understand the origin of the discrepancy between our results and shock wave experiments, we calculated the thermodynamic properties of Fe along the Hugoniot equation of state, defined as (*33*)

$$\frac{1}{2}(P + P_0)(V_0 - V) = U - U_0 \qquad (1)$$

where one assumes that Fe is shocked from a state where pressure is P_0, atomic volume is V_0, and its internal energy per atom (potential and kinetic) is U_0, to a state where these are P, V, and U, respectively. We determined the values of V and T that fulfill Eq. 1 in a set of pressures ranging from 100 to 400 GPa (*34*). At a given P, T is varied until V and U, as calculated with the OP method (*35*) satisfy Eq. 1. The Hugoniot relation (Eq. 1) can easily be generalized to include the possibility of the coexistence of the liquid and solid phases (*33*). In particular, if a system at *P-T* conditions lies in the coexistence line of phases A and B (the melting line in the case of solid and liquid coexistence), the volume and the internal energy of the two phases have to be weighted with their relative molar proportions x_A and $1 - x_A$, so that Eq. 1 reads

$$\frac{1}{2}(P + P_0)[V_0 - x_A V_A - (1 - x_A)V_B] = x_A U_A + (1 - x_A)U_B - U_0 \qquad (2)$$

If Eq. 2 admits a solution with $0 < x_A < 1$ at pressure P, then the system displays phase coexistence. The shocked Fe remains solid up to 200 (±20) GPa (Fig. 3). By further increasing pressure, the additional energy provided by the impact is partially absorbed by the system in terms of heat of melting, which progressively increases the relative molar fraction of melted Fe. In this regime, in fact, Eq. 2 admits a solution with $0 < x_A < 1$, indicating that the solid (A) and the liquid (B) phases coexist, and the system lies on the

melting line. The melting regime along the Hugoniot equation of state ends at a pressure of 280 (±20) GPa, above which Fe is completely melted. The density and the sound velocity (*36*) of Fe along the Hugoniot relation are compared with experimental data in Fig. 3, A and B. The agreement with experiments is satisfactory in the solid and in the liquid phase. In the regime of phase coexistence (200 to 280 GPa), the sample is not homogeneous, and sound velocities cannot be extracted from elastic theory.

Our simulations also provide an accurate determination of the temperature along the Hugoniot equation of state at all pressures, in the liquid and in the solid regime (Fig. 3C). Unlike pressure and density, the reliability of temperature determinations in a shock wave experiment on metallic systems is still controversial (*37, 38*). In the solid portion of the Hugoniot equation of state, our values agree with tight-binding calculations (*39*) and with Brown and McQueen's estimates based on reasonable thermodynamic parameters (*1*). Instead, temperatures measured in shock wave experiments are systematically higher than ours in the solid portion of the Hugoniot equation. This may be traced to difficulties in directly measuring the temperature of a shocked sample.

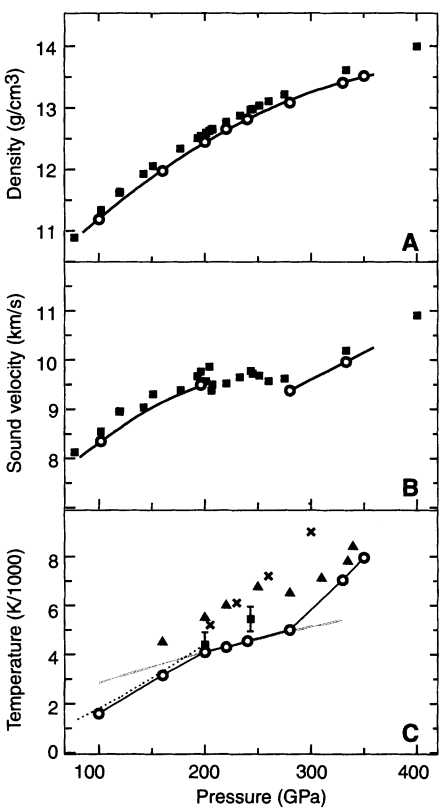

Fig. 3. (**A**) Density, (**B**) sound velocity, and (**C**) temperature along the Fe Hugoniot equation of state. Circles represent our results (lines are a guide to the eye). Squares and the dotted curve in (C) show Brown and McQueen's data (*1*). Triangles show data from (*4*), and crosses show data from (*2*). The gray curve in (C) represents our melting line. Bars in (C) represent errors as estimated in (*1*).

Moreover, our calculations suggest a reinterpretation of Brown and McQueen's data for sound velocities (*1*). We propose that the first kink (at 200 GPa) in Brown and McQueen's data is related to melting rather than to a solid-solid transition. Brown and McQueen's Hugoniot equation of state would then intercept the melting line at ~200 GPa and ~4200 K, in agreement with the DAC melting results (*3*), thus reconciling Brown and McQueen's shock wave measurements with static DAC data. According to this reinterpretation, the second kink observed by Brown and McQueen is not associated with a phase transition, but may rather be a by-product of the phase coexistence between the solid and the liquid, as suggested by MD simulations performed on Ar by Belonoshko (*40*), and thus be dependent on experimental conditions. This scenario would be confirmed by the recent repetition of Brown and McQueen's experiment, by Nguyen and Holmes (*41*), where the second kink was not observed. It should be noted, however, that Brown and McQueen's estimate of T_m, based on the second kink in the sound velocity curve, is compatible with our melting line, within the mutual uncertainties.

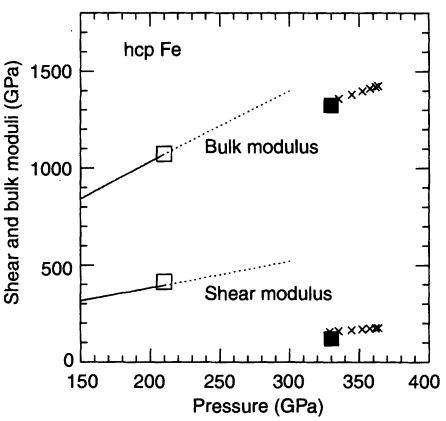

Fig. 4. Voigt averages (*47*) of shear and bulk moduli for compressed solid Fe, as compared with inner-core data and DAC experiments. Curves show room-temperature DAC data (*14*) (solid curve, actual data; dashed curve, extrapolation). Open squares show room temperature data from this work, crosses represent seismic observations for the inner core (*47*), and solid squares show the melting temperature data from this work. Theoretical values were computed with OPs, at high temperature by long classical runs (500 ps) (*45*) on solid samples of 1000 atoms and at low temperature by finite-strain methods (*13*). The size of the squares represents the error bars discussed in the text.

Our theory also provides information on the thermodynamic, elastic, and diffusion properties of Fe at ICB conditions. At 330 GPa, the calculated density decrease ($\Delta\rho/\rho$) upon melting of Fe is 1.6%. The enthalpy of melting (ΔH_m) and the entropy of melting found at 330 GPa are 0.7×10^6 J/kg and $0.86k_B$, respectively (*42*). ΔH_m is smaller than previously suggested (*10, 37*), except for estimates based on dislocation theory (*43*). With our value for ΔH_m, the contribution to the geodynamo energy budget of the freezing of Fe in the liquid outer core should be smaller than suggested (*10*), or alternatively, the age of the inner core should be shorter (*44*).

Our calculated room-temperature elastic constants (Table 1) are consistent with full ab initio calculations (*13*) and with the recently revised DAC data (*14*). We estimated a shear viscosity of the liquid at T_m of 1.3 (±0.1) × 10^{-2} Pa, in agreement with recent calculations (*17*). For the solid, we calculated the bulk and the shear moduli of hcp Fe at T_m, and they matched the compressional and the shear wave seismic data for the inner core (Fig. 4). For the compressional wave velocity, we calculated an anisotropy of <10% [only an upper bound can be provided because of the uncertainty in the calculated elastic constants (*45*)]. If we were to attribute the observed anisotropy of the inner core extracted from the seismic data to the partial alignment of hcp Fe grains along Earth's rotational axis, we would estimate a degree of alignment >30%, in line with recent suggestions (*13*). The shear modulus estimated from seismic data in the solid inner core is anomalously low for a close-packed phase, leading to suggestions that additional low shear wave phases may be present there, other than hcp Fe (*14, 24*). Usually, the shear modulus at the melting point of most solid metals shows, at zero pressure, a reduction of <50% from its low-temperature value (*46*). The inner-core

Table 1. Comparison of elastic constants (*C*) and Voigt (*47*) averages of shear (S_v) and bulk moduli (B_v) of Fe as obtained with OP at P = 210 GPa and T = 300 K with full ab initio results of (*13*) and DAC experiments of (*14*). All values are given in GPa. The errors due to the OP procedure (*23*) are estimated to be <5%. Our results agree within 9% with full ab initio results (*13*). The agreement with experiment (*14*) on the individual elastic constants is poorer (34% in the worst case). Yet, the angular averages (B_v and S_v) agree, and our shear anisotropies follow the correct trends shown in (*13*).

Results	Elastic constants					B_v	S_v
	C_{11}	C_{12}	C_{33}	C_{13}	C_{44}		
Theoretical, OP	1554	742	1796	820	414	1074	414
Theoretical, ab initio (*13*)	1697	809	1799	757	421	1085	445
Experimental, DAC (*14*)	1533	846	1544	835	583	1071	396

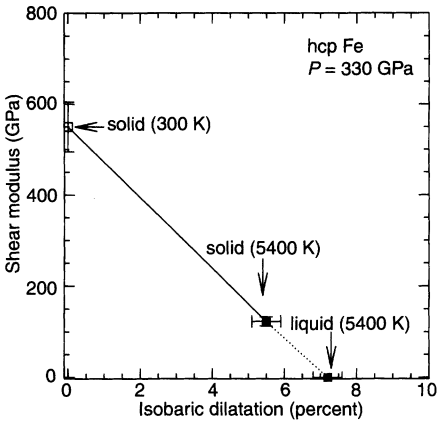

Fig. 5. Behavior of the shear modulus of hcp Fe as a function of the isobaric thermal dilatation. The open square represents x-ray diffraction measurements (*14*), and the solid squares show theoretical results. The lines are guides to the eye.

shear modulus (*47*) displays a 70% reduction with respect to low-temperature measurements (*14*) and calculations (*13*) in pure Fe. Our calculated shear modulus of hcp Fe close to melting is compatible with the seismic data (Fig. 4). This decreased shear modulus fits a Born-Durand model of melting (*46*). According to this model, the isobaric thermal dilatation within the solid phase and after melting is linearly correlated with the decrease of the shear modulus. This empirical law has been verified in a large class of systems, ranging from molecules to metals (*46*). The shear modulus of Fe closely follows the Born-Durand law (Fig. 5), even if, in comparison with standard metals, compressed Fe melts much closer to the mechanical instability (vanishing shear modulus), which correlates with the small volume increase at melting.

The density of liquid Fe at 330 GPa and 5400 K is estimated to be 12.80 g/cm^3. Its difference with the preliminary reference Earth model value for Earth's outer core [12.166 g/cm^3 (*47*)] is ~5 to 6%, consistent with the values currently assumed in geophysical models (~7%) (*10*). Moreover, for solid Fe at 330 GPa and 5400 K, we find a density of 13.0 g/cm^3, ~2 to 3% larger than the density of the inner core at the ICB [12.76 g/cm^3 (*47*)], supporting the possible presence of lighter elements also in the inner core (*7*).

References and Notes

1. J. M. Brown and R. G. McQueen, *J. Geophys. Res.* **91**, 7485 (1986).
2. Q. Williams, R. Jeanloz, J. Bass, B. Svendsen, T. J. Ahrens, *Science* **236**, 181 (1987).
3. R. Boehler, *Nature* **363**, 534 (1993).
4. C.-S. Yoo *et al.*, *Phys. Rev. Lett.* **70**, 3931 (1993).
5. S. K. Saxena, G. Shen, P. Lazor, *Science* **264**, 405 (1994).
6. A. Shen *et al.*, *Geophys. Res. Lett.* **25**, 373 (1998).
7. A. Jephcoat and P. Olson, *Nature* **325**, 332 (1987).
8. R. Jeanloz, *Annu. Rev. Earth Planet. Sci.* **18**, 357 (1990).
9. W. A. Bassett, *Science* **266**, 1662 (1994); J. P. Poirier, *Phys. Earth Planet. Inter.* **85**, 319 (1994).
10. F. Stacey, *Physics of the Earth* (Brookfields, Brisbane, Australia, 1992).
11. A. M. Dziewonski and F. Gilbert, *Nature* **234**, 465 (1971).
12. J. Tromp, *Nature* **366**, 678 (1993), and references therein.
13. L. Stixrude and R. E. Cohen, *Science* **267**, 1972 (1995); G. Steinle-Neumann, L. Stixrude, R. Cohen, *Phys. Rev. B* **60**, 791 (1999).
14. H.-K. Mao *et al.*, *Nature* **396**, 741 (1998); **399**, 280 (1999) (erratum).
15. D. A. Boness and J. M. Brown, *J. Geophys. Res.* **95**, 21721 (1990).
16. P. Söderlind *et al.*, *Phys. Rev. B* **53**, 14063 (1996).
17. G. A. de Wijs *et al.*, *Nature* **392**, 805 (1998).
18. N. Mermin, *Phys. Rev.* **137**, A1441 (1965); A. D. Becke, *Phys. Rev. A* **38**, 3098 (1988); J. P. Perdew, *Phys. Rev. B* **33**, 8822 (1986).
19. Ab initio calculations were performed using a plane wave basis set with an energy cutoff of 100 rydbergs (Ry), Γ-point (k = 0) sampling of the Brillouin zone, and cells of 64 atoms. Convergence tests show that the results are unchanged by increasing the energy cutoff to 120 Ry and the cell size up to 128 atoms. Failure to include the semicore states 3s and 3p in the Fe pseudopotential would give an approximately +80-GPa disagreement with experimental data on the equation of state (*20*).
20. H.-K. Mao *et al.*, *J. Geophys. Res.* **95**, 21737 (1990).
21. A. B. Belonoshko and R. Ahuja, *Phys. Earth Planet. Inter.* **102**, 171 (1997).
22. M. I. Baskes, *Phys. Rev. B* **46**, 2727 (1992).
23. The classical potential at a given *P-T* point is constructed with the following iterative procedure: A trial many-body interparticle potential V_0 (*21*, *22*) is used to produce an MD trajectory for 64 particles in the isothermal-isobaric ensemble at *P-T* conditions; the density ρ_0, averaged on this trajectory, is calculated. In the resulting configuration, first-principles stress and forces are computed, and a new potential V_1 is generated by fitting these forces and stress (forces within 5% and stress within 1%). The configuration is then evolved with V_1, still at *P-T* conditions, and a new average density ρ_1 is calculated. If $|\rho_1 - \rho_0|/\rho_0 < \delta\rho$, where $\delta\rho$ is a threshold parameter, the classical potential V_1 generated in this way is accepted as optimal at the given *P-T* conditions, otherwise the procedure is iterated. We have found that, if $\delta\rho = 5 \times 10^{-3}$, the OP gives values that are unchanged by further iteration not only for the density, but also for a set of thermodynamical observables (such as the elastic constants, diffusion coefficients, and viscosity). The required accuracy can be achieved with potentials with different parameters or even different functional form [provided that they include a two-body and a density-dependent many-body angular part (*21*, *22*)], giving rise to a class of OPs at any given *P-T* condition.
24. M. Matsui and O. L. Anderson, *Phys. Earth Planet. Inter.* **103**, 55 (1997).
25. D. Alfè, M. J. Gillan, G. D. Price, *Nature* **401**, 462 (1999).
26. A. Laio *et al.*, in preparation. First-principles pseudopotential calculations on Al have been performed within LDA and a 12-Ry energy cutoff. Convergence tests on cell size show that T_m of Al is unchanged within 30 K when the cell size is increased from 64 to 256 atoms. Errors for Al do not include those due to the LDA.
27. The melting temperature T_m at pressure P is calculated by a solid-liquid coexistence method [O. Tomagnini *et al.*, *Phys. Rev. Lett.* **76**, 1118 (1996)] applied on classical potentials that are optimal at *P-T*$_m$ conditions. Because T_m is not known a priori, it is determined by the following iterative procedure. Starting from a trial melting temperature T_m^0, an OP is determined at *P-T*$_m^0$, the melting temperature T_m^1 of this potential is computed, a new OP is determined at *P-T*$_m^1$, and the procedure is iterated i times, until $T_m^i = T_m^{i-1}$. In proximity of the melting point, OPs can be generated by this procedure either from liquid trajectories only, from solid trajectories, or from both liquid and solid trajectories. We found that T_m is the same, within our OP error bar (±100 K for Fe at ICB), in all three cases. We also checked that T_m is unaffected by the choice of T_m^0. Errors in T_m due to the number of particles (up to 6000) and finite simulation times were checked and estimated to be smaller than the error bars.
28. E. A. Brandes, Ed., *Smithells Metals Reference Book* (Butterworths, London, ed. 6, 1983); D. R. Lide, Ed., *CRC Handbook of Chemistry and Physics* (CRC Press, Boca Raton, FL, ed. 74, 1993).
29. J. F. Cannon, *J. Phys. Chem. Ref. Data* **3**, 781 (1974).
30. G. A. de Wijs, G. Kresse, M. J. Gillan, *Phys. Rev. B* **57**, 8223 (1998).
31. M. P. Allen and D. J. Tildsley, *Computer Simulation of Liquids* (Clarendon, Oxford, 1987).
32. An alternative way to estimate errors arising from the OP modeling consists in constructing, at each *P-T* condition, several OPs differing in the parameters or even in the functional form (*23*). The error bars are then estimated as the spread in the values of the observables as calculated with these OPs. Following this, errors due to the OP method on T_m and on density for Fe at ICB conditions are of the order of ±100 K and 0.05 g/cm^3, respectively.
33. R. G. McQueen, S. P. Marsh, J. W. Taylor, J. N. Fritz, W. J. Carter, in *High Velocity Impact Phenomena*, R. Kinslow, Ed. (Academic Press, New York, 1970), pp. 293–417.
34. The initial state, labeled "0" in Eq. 1, is, in our calculation, body-centered cubic Fe at P = 0 and T = 0 (*39*). V_0 and U_0 are the ab initio volume and total energy at P = 0 and T = 0, respectively (V_0 = 11.4 Å^3/atom). We also checked that the small (~3%) difference between the theoretical and experimental V_0 does not significantly affect our results at high pressure (the temperature at 200 GPa on the Hugoniot equation of state would be ~150 K higher if the experimental V_0 was used).
35. The OP internal energy U_{OP} is calculated as a time average on a 30-ps MD trajectory at full convergence with respect to cell size (up to 2000 particles). The internal energy U is then referred to the first-principles energy scale as $U = U_{OP} - (U_{OP}^{ref} - U_{ai}^{ref})$, where U_{OP}^{ref} and U_{ai}^{ref} are the instantaneous values of OP and first-principles internal energies of an ab initio configuration at the *P-T* conditions of interest, respectively. It has been checked that the difference $U_{OP}^{ref} - U_{ai}^{ref}$ does not depend on the chosen instantaneous configuration.
36. Sound velocities along the Hugoniot equation of state are computed from the adiabatic elastic constants in the solid and from the adiabatic compressibility in the liquid (*45*).
37. O. L. Anderson and A. Duba, *J. Geophys. Res.* **102**, 22659 (1997).
38. R. Boehler, *Philos. Trans. R. Soc. London Ser. A* **354**, 1265 (1996).
39. L. Stixrude, E. Wasserman, R. E. Cohen, *J. Geophys. Res.* **102**, 24729 (1997).
40. A. B. Belonoshko, *Science* **275**, 955 (1997).
41. J. H. Nguyen and N. C. Holmes, abstract We H3-62, paper presented at the International Conference on High Pressure Science and Technology (AIRAPT-17), Honolulu, HI, 25 to 30 July 1999.
42. It follows from our discussion of the errors on T_m that the errors on ΔH_m and ΔS are $\pm 0.05 \times 10^6$ J/kg and $\pm 0.06 k_B$, respectively.
43. J.-P. Poirier and T. J. Shankland, *Geophys. J. Int.* **115**, 147 (1993).
44. Our values for ΔH_m, $\Delta\rho$, and the slope of the melting line ($dT_m/dP \simeq$ 10 K/GPa) fulfill the Clausius-Clapeyron equation.
45. M. Parrinello and A. Rahman, *J. Chem. Phys.* **76**, 2662 (1982).
46. J. L. Tallon, *Philos. Mag. A* **39**, 151 (1979).
47. A. M. Dziewonski, *Phys. Earth Planet. Inter.* **25**, 297 (1981).

48. We thank C. Cavazzoni for technical support in code development. This research was partially supported by Ministero dell'Università e della Ricerca Scientifica e Tecnologia and Istituto Nazionale per la Fisica della Materia. S.B. acknowledges European Commission partial support through the ICARUS2 project at CINECA.

17 November 1999; accepted 21 December 1999